Supporting Information for "The Intrinsic Activity Descriptor of TM-N$_3$-C Single Atom Catalysts for Electrochemical CO$_2$ Reduction: a DFT Study"

Linmeng Wang[a], Zhiyuan Liu[a], Rushuo Li[a], Hongyi Gao[a, b*], Ping Yang[c*], Wei Wang[c], Xiangdong Xue[a], Shihao Feng[a], Lingjing Yu[a], Ge Wang[a*]

[a] Beijing Advanced Innovation Center for Materials Genome Engineering, Beijing Key Laboratory of Function Materials for Molecule & Structure Construction, School of Materials Science and Engineering, University of Science and Technology Beijing, Beijing 100083, PR China

[b] Shunde Innovation School, University of Science and Technology Beijing, Shunde 528399, P. R. China

[c] Sinopec Research Institute of Petroleum Processing Co., Ltd., Beijing 100083, China

Corresponding authors: Hongyi Gao, E-mail: hygao@ustb.edu.cn, Ping Yang, E-mail: yangp.ripp@sinopec.com, Ge Wang, E-mail: gewang@ustb.edu.cn

1   Computational details

The geometry structures, electronic structure, free energy, adsorption energy, atomic charge, and crystal orbital Hamilton population COHP were calculated by the spin-polarized DFT via the Dmol3 package in Material Studio software.[1] The linear combination of atomic orbital method (LCAO) method was applied for describe the electronic state of the system. Furthermore, the generalized gradient approximation (GGA) functional in the form of Perdew-Burke-Ernzerhof (PBE) were used to correct exchange-correlation energy.[2] The empirical correction in the form of Grimme's scheme (DFT-D) was employed to describe long-range van der Waals interaction.[3] Balancing time-consuming and accuracy, for TM atoms, the core treatment method of DFT semi-core pseudopotential (DSSP) was selected to employ a single effective potential to replace core electrons which treating with the relativistic corrections, when other atoms (such as H, C, N, and O) were calculated with all electron method.[4–6] The basic set of double numerical plus polarization (DNP) has enough quality for SACs, and the smearing was set to 0.005 Ha to achieve precise electronic convergence. The vacuum layer thickness of 20 Å were constructed in the 36 $TM-N_3-C$ (TM-I and TM-II, TM = Ti, V, Cr, Mn, Fe, Co, Ni, Cu, Zn, Zr, Nb, Mo, Tc, Ru, Rh, Pd, Ag, Cd) slab models, which break periodic images along z axis to avoid pseudo-interaction.[7,8] The cutoff energy and k-point grid was set as 570 eV and $3 \times 3 \times 1$, respectively.[7,8] The convergence tolerance of energy, maximum displacement, maximum force were set as 10^{-5} Ha, 0.005 Å, and 0.002 Ha /Å, respectively.[4,5] It's worthy noticing that the total magnetic moment of SACs catalysts is non-negligible owing to the transition metal

atoms embedded on the graphene sheet, although N (pyridinic or pyrrolic) doped carbon catalysts are non-magnetic and closed-shell systems. The initial value of magnetism is briefly assessed using crystal field theory, and the total magnetic moment of TM-N_3-C systems is derived after unrestricted (spin-polarized) density functional theory calculations, as summarized in Figure S1, in agreement with the prior study for the similar systems.[8–12] Furthermore, the convergence test of the magnetic state for TM-N_3-C were experimented through the different origin of magnetism in spin-polarized DFT calculations and the results indicate that the magnetic ground states are stable in this work (Figure S2).

The atomic charge of TM centers and charge transfer with adsorbed species were derived from the Hirshfled[13] method. The energy and the adsorption Gibbs free energy of the adsorbed species on the TM-N_3-C substrate are defined as follows[9,14]:

$$E_{ads} = E(* ads) - E(*) - E(adsorbate)$$

$$G_{ads} = G(* ads) - G(*) - G(adsorbate)$$

where E (*ads), G (*ads), E (adsorbate), G (adsorbate), E (*), and G (*) represent the total energies or Gibbs free energy of the adsorbates on catalysts surfaces, the catalysts, and the isolated adsorbed species (i.e., CO_2 and H_2). For electrocatalytic CO_2 reduction to CH_4 (CO_2-to-CH_4), involving eight PCET steps, it produces vast reaction intermediates and may be accompanied with HER. Based on Nørskov's study, the Gibbs free energy changes were calculated by the computational hydrogen electron (CHE) model for all possible elementary reaction steps in the electrochemical CO_2RR process.[15] To reveal the optimal reaction pathway, RDS, and U_L, the Gibbs free energy

changes (ΔG) of each elementary step is expressed by the following functional:

$$\Delta G = \Delta E - T\Delta S + \Delta E_{ZPE} + \Delta \int C_p dT + \Delta G_{pH} + \Delta G_U$$

in which ΔE, ΔE_{ZPE}, ΔS, and $\Delta \int C_p dT$ denote the differences of the electronic energy, zero-point energy (ZPE), entropy, and heat capacity between reactants and production in elementary reaction step, respectively. Moreover, ΔG_{pH} means the contribution of H^+ concentration changes for reaction free energy and is assessed by the following equation: $\Delta G_{pH} = -2.303 \times k_B T \times pH$ (k_B is the Boltzmann constant of 1.38×10^{-23} J/K). Additionally, ΔG_U is the free energy determined by electrode potential, which is expressed by $\Delta G_U = neU$ (n represents the number of electrons transferring from reactant in each step and U means the electrode potential, respectively). In this work, the values of T, pH, and U were set to 298.15K, 0, and 0 V vs. SHE, respectively. Furthermore, the thermodynamic data at 298.15K of the isolated adsorbates, such as CO, HCOOH, CH_3OH, and CH_4, were obtained from NIST database. In addition, U_L, depending on RDS, can be calculated by the following functional:

$$U_L = -\Delta G_{max}/e$$

where ΔG_{max} means the maximum Gibbs free energy change in all elementary reaction steps for the CO_2-to-CH_4.

Significantly, the primary property of electrocatalysts is the thermodynamic stability of TM embedded on N_3-C to avoid the single atom aggregating on the substrate, which can be assessed by the binding energy (E_{bind}) and cohesive energy (E_{coh}).[8,9] In specific, they were investigated to estimate the interaction between TM atom and N_3-C substrate using the following equations:[8,9]

$$E_{bind} = E_{TM-N_3-C} - E_{N_3-C} - E_{TM}$$

$$E_{coh} = E_{TM-bulk}/N - E_{TM}$$

Where E_{TM-N_3-C}, E_{N_3-C}, E_{TM}, $E_{TM-bulk}$ are defined as the total energy of TM-N$_3$-C, N$_3$-C, single TM atom in the vacuum, and TM atoms in bulk crystal, respectively, and N denotes the number of TM atoms in the unit cell. Based on previous studies, the formation of single TM atoms on N doped carbon substrate is thermodynamically favorable when the difference between E_{bind} and E_{coh} ($E_{bind} - E_{coh}$) is less than 0 eV. On the contrary, when the value of $E_{bind} - E_{coh}$ is positive, it indicates that the bonding between the metal atom and the substrate is less strong enough to form dispersive single-atomic moieties.[8,9] In this work, we further investigate the electrochemical stability of TM-SAs in TM-N$_3$-C systems and here calculate the dissolution potential (Udiss) based on the formalism proposed by Greely et al., shown as following:[16]

$$U_{diss} = U_{diss}^0 - (E_{TM-N_3-C} - E_{N_3-C} - \mu_{TM-bulk})/ne$$

where U0 diss is the standard dissolution potential of a pure TM, listed and summarized in the relative studies,[7,17–19] E_{TM-N_3-C} and E_{N_3-C} mean the total energies of TM-N$_3$-C and N$_3$-C, respectively. $\mu_{TM-bulk}$ is the chemical potential of a TM atom in its most stable bulk phase, and n represents the number of transferred electrons in the metal-dissolution process.
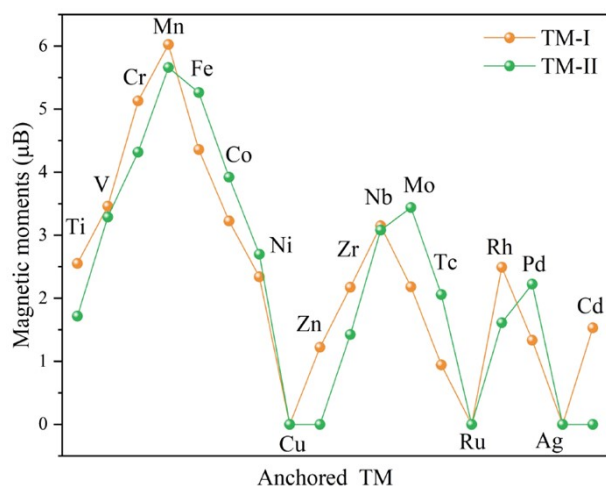
2　Results and discussion

Figure S1. Magnetic moments of TM-N_3-C systems, in which the total magnetic moments are derived from the spin populations of TM-N_3-C SACs.
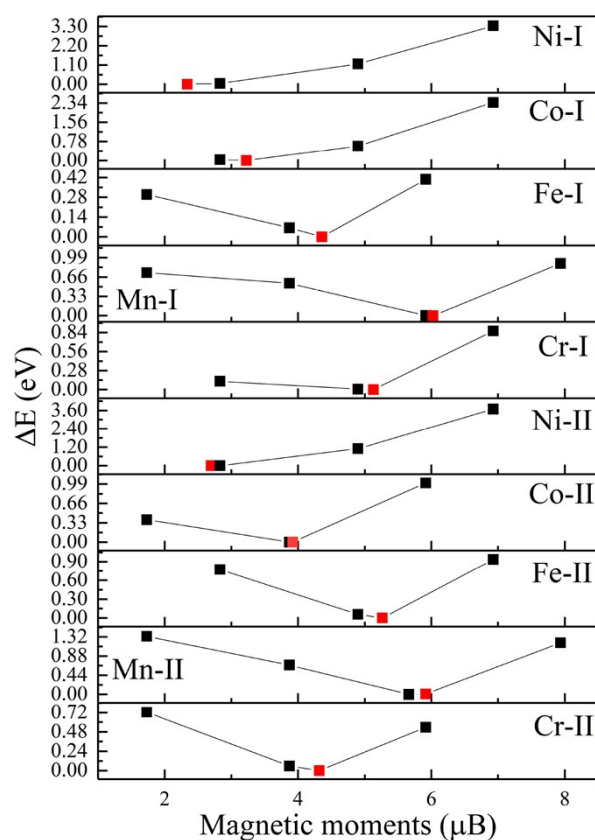

Figure S2. The relationships between total energies of TM-N_3-C catalysts and their magnetic moments and emphasizing the red points sites at the bottom of curves, representing that the TM-N_3-C with corresponding magnetic moment is stable ground
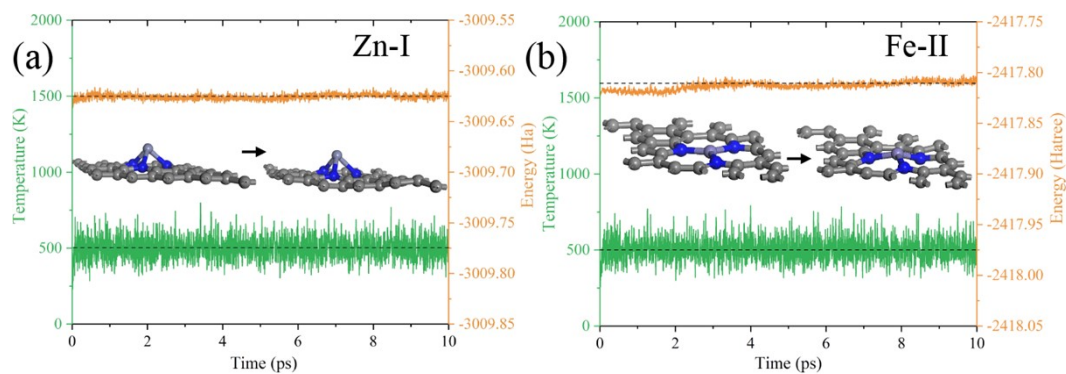
state and the total energy is set as 0 eV.

Figure S3. Variations of energies for AIMD simulations of (a)Zn-I and (b)Fe-II. Insets show the changes in the corresponding geometry configurations after AIMD simulations compared to the initial structures.
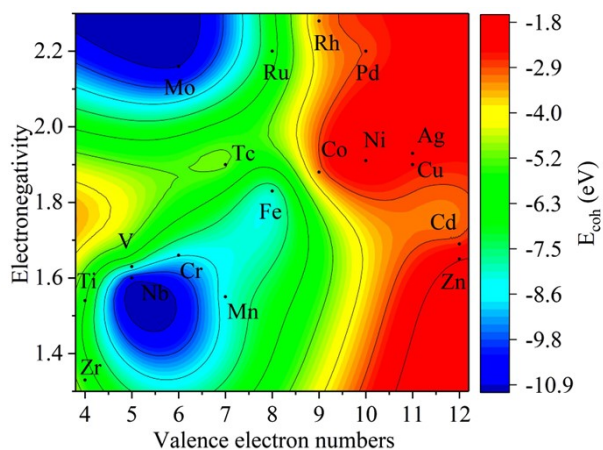

Figure S4. The cohesive energy map for TM atoms as a function of outer-shell electrons number and electronegativity.
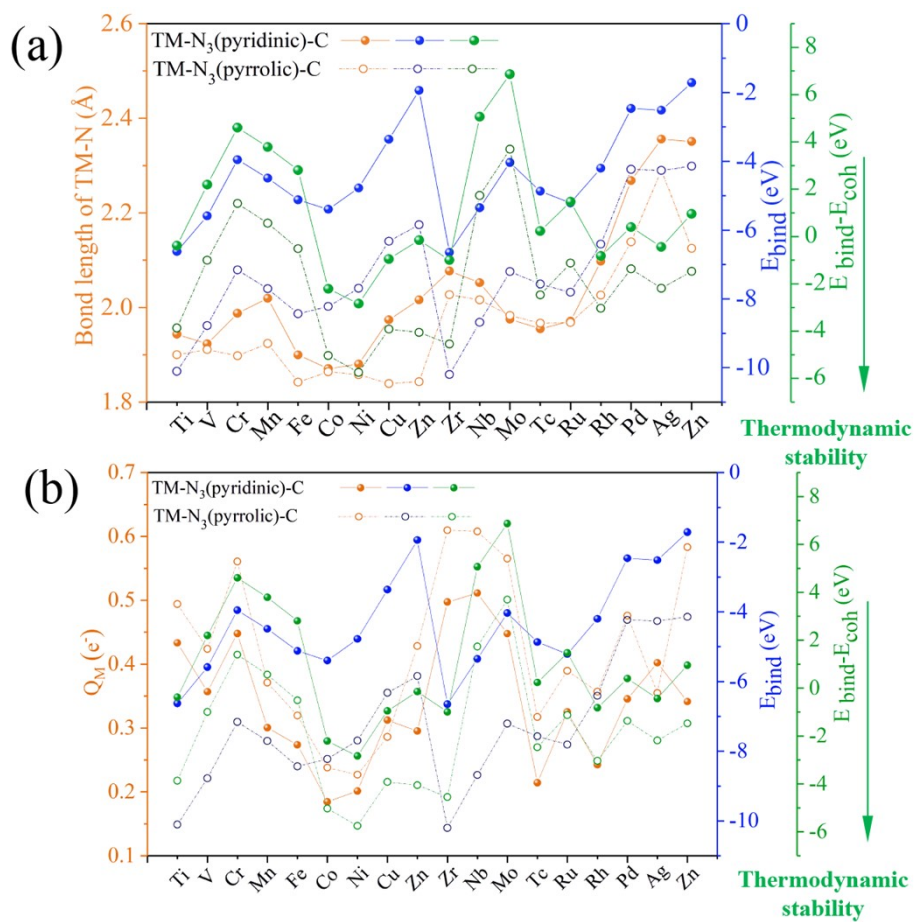
Figure S5. (a) The bond length of TM-N or (b) the Hirshfeld charge of metal atoms, corresponding E_{bind}, and E_{bind}-E_{coh} of TM-N$_3$-C catalysts.
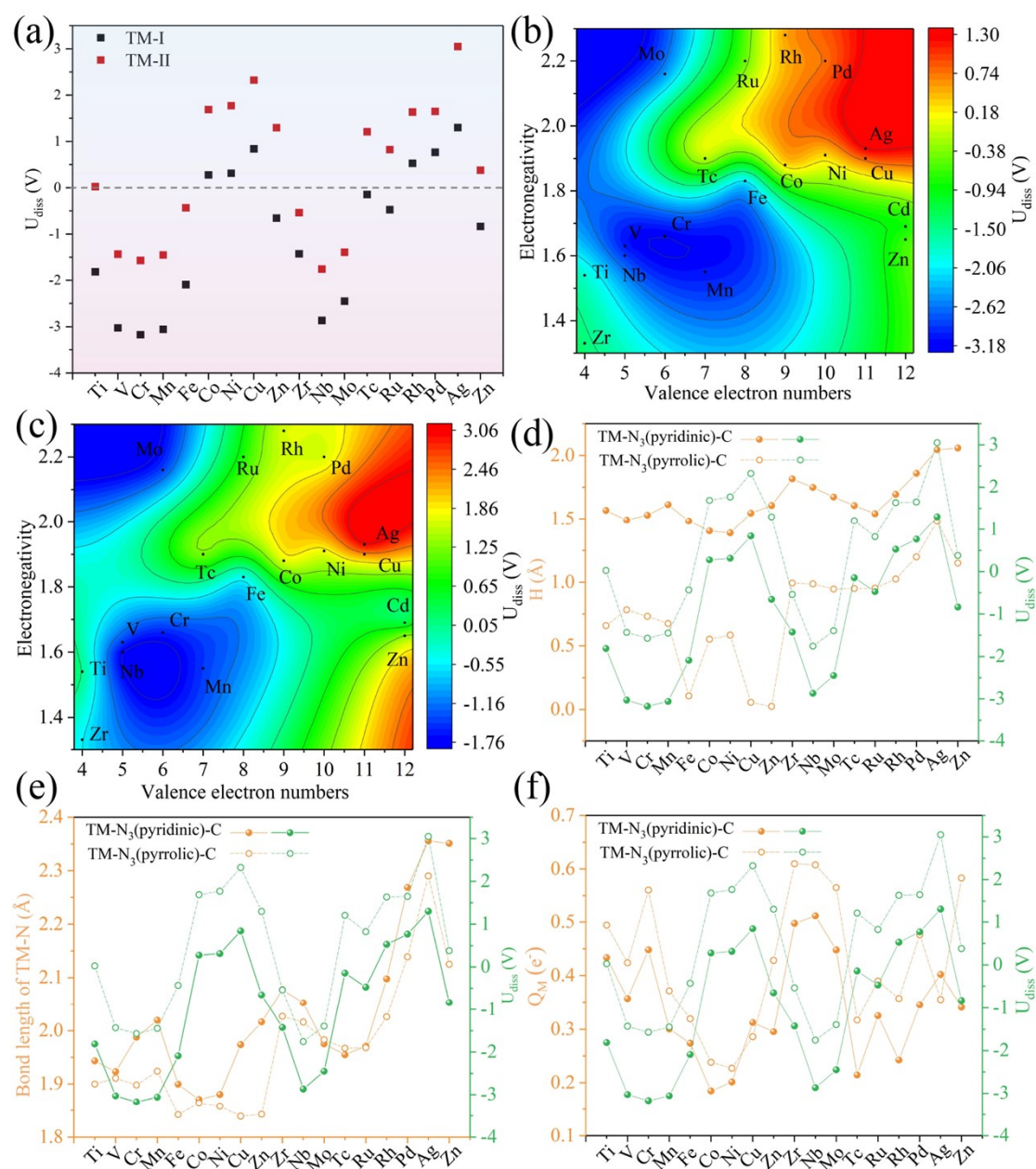
Figure S6. (a) Electrochemical stability of SACs in term of the dissolution potential (U_{diss}) of TM atoms for TM-N_3-C systems. The dissolution potential (U_{diss}) maps for (b) TM-N_3(pyridinic)-C and (c) TM-N_3(pyrrolic)-C as a function of outer-shell electrons number and electronegativity of metal atoms. The point-fold line charts displaying the (d) H, (e) d, (f) QM of TM-N_3-C systems and the corresponding U_{diss}.

Table S1. The inherent characteristics of TM-N$_3$-C involving the bond length of TM-N, the elevation altitude from TM center to N$_3$-C substrate, and the Hirshfeld charge of metal active sites.

TM-N$_3$-C SACs	d (Å)	H (Å)	Q$_M$ (e$^-$)
Ti-I	1.943	1.566	0.433
V-I	1.923	1.490	0.357
Cr-I	1.988	1.529	0.448
Mn-I	2.019	1.612	0.300
Fe-I	1.900	1.483	0.274
Co-I	1.870	1.404	0.184
Ni-I	1.880	1.388	0.201
Cu-I	1.974	1.546	0.312
Zn-I	2.016	1.605	0.295
Zr-I	2.077	1.815	0.497
Nb-I	2.052	1.748	0.511
Mo-I	1.975	1.673	0.448
Tc-I	1.955	1.605	0.214
Ru-I	1.971	1.541	0.325
Rh-I	2.0985	1.693	0.242
Pd-I	2.268	1.859	0.346
Ag-I	2.356	2.044	0.402
Cd-I	2.351	2.058	0.341
Ti-II	1.900	0.658	0.494
V-II	1.911	0.783	0.424
Cr-II	1.898	0.732	0.561
Mn-II	1.924	0.675	0.371
Fe-II	1.842	0.107	0.320
Co-II	1.864	0.552	0.238
Ni-II	1.858	0.585	0.227
Cu-II	1.839	0.056	0.286
Zn-II	1.843	0.024	0.428
Zr-II	2.027	0.993	0.610
Nb-II	2.016	0.986	0.608
Mo-II	1.983	0.946	0.565
Tc-II	1.967	0.950	0.317
Ru-II	1.968	0.953	0.390
Rh-II	2.026	1.025	0.357
Pd-II	2.139	1.199	0.476
Ag-II	2.290	1.481	0.355
Cd-II	2.125	1.151	0.5831

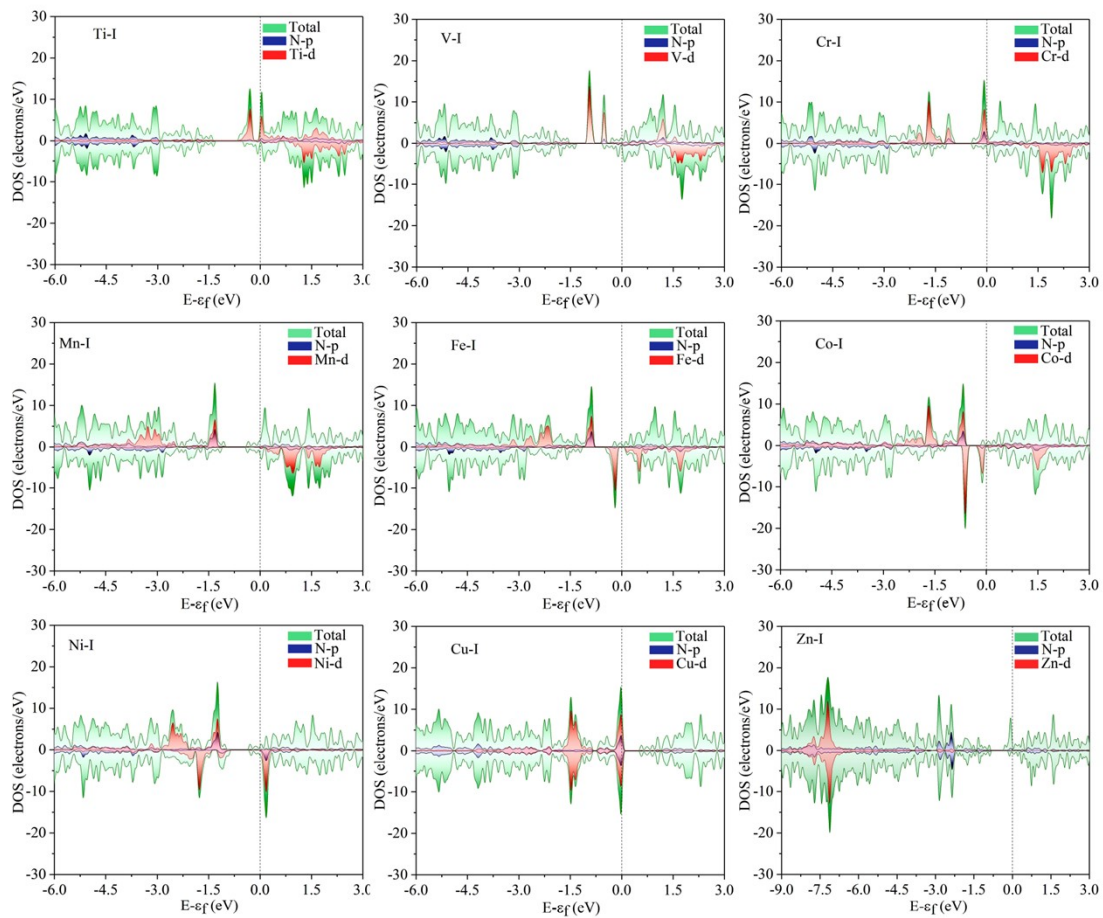Figure S7. The density of states (DOS) projected onto 3d TM-d and N-p orbitals and total density of states (TDOS) of TM-N$_3$(pyridinic)-C (TM-I) electrocatalysts.
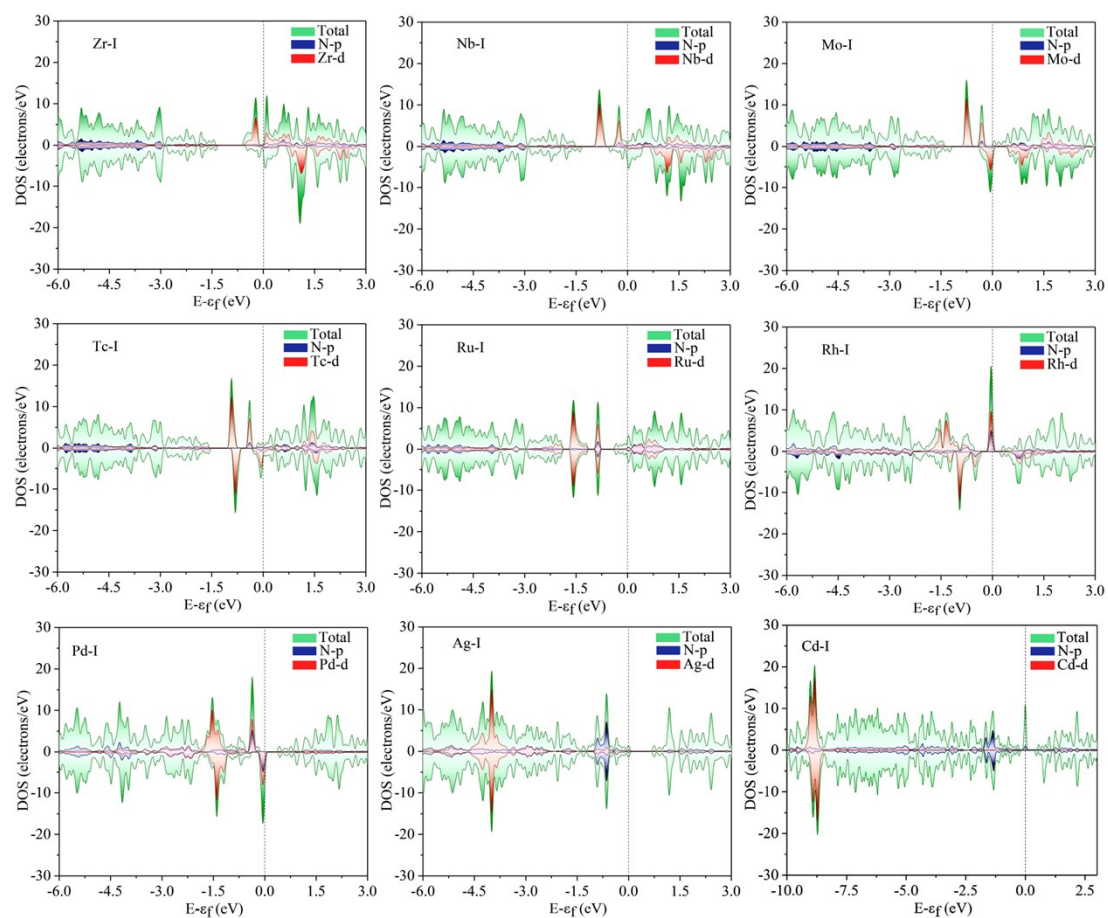
Figure S8. The DOS projected onto 4d TM-d and N-p orbitals and TDOS of TM-N$_3$(pyridinic)-C (TM-I) electrocatalysts.
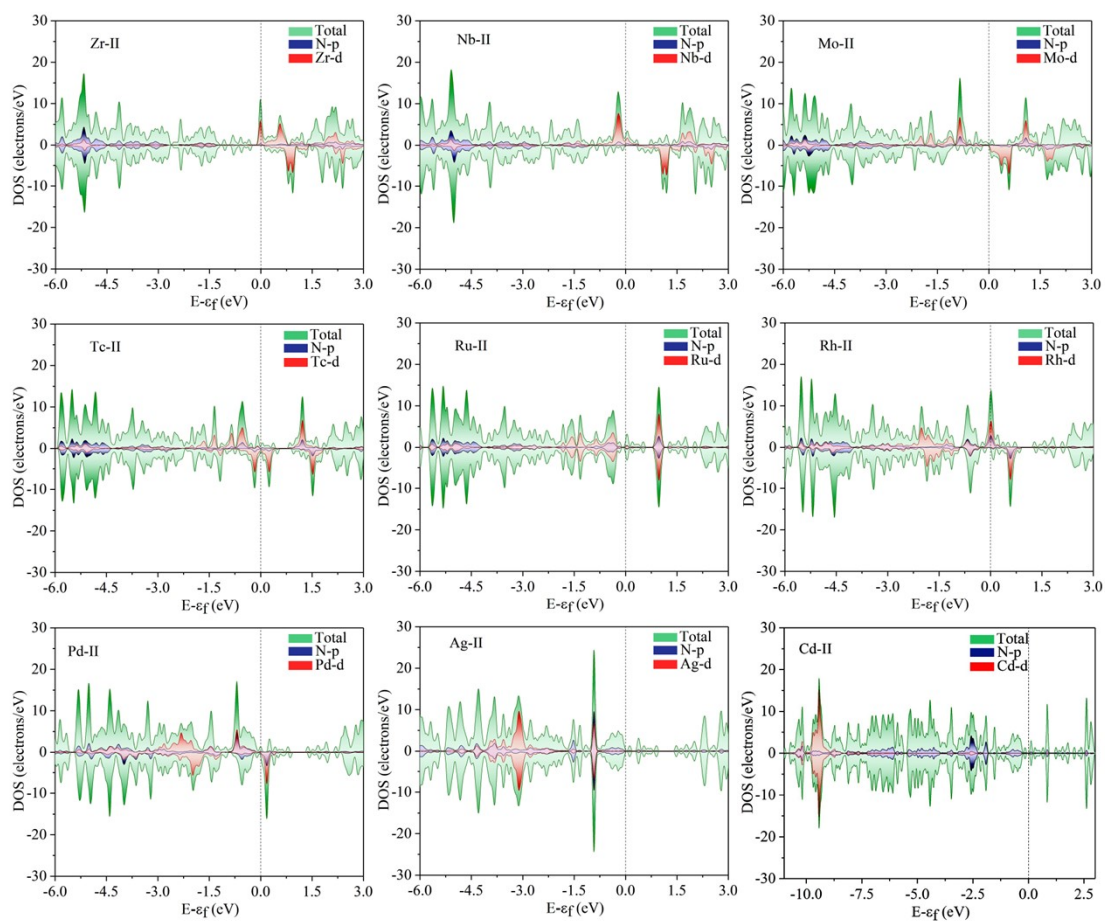
Figure S9. The DOS projected onto 3d TM-d and N-p orbitals and TDOS of TM-N$_3$(pyrrolic)-C (TM-II) electrocatalysts.
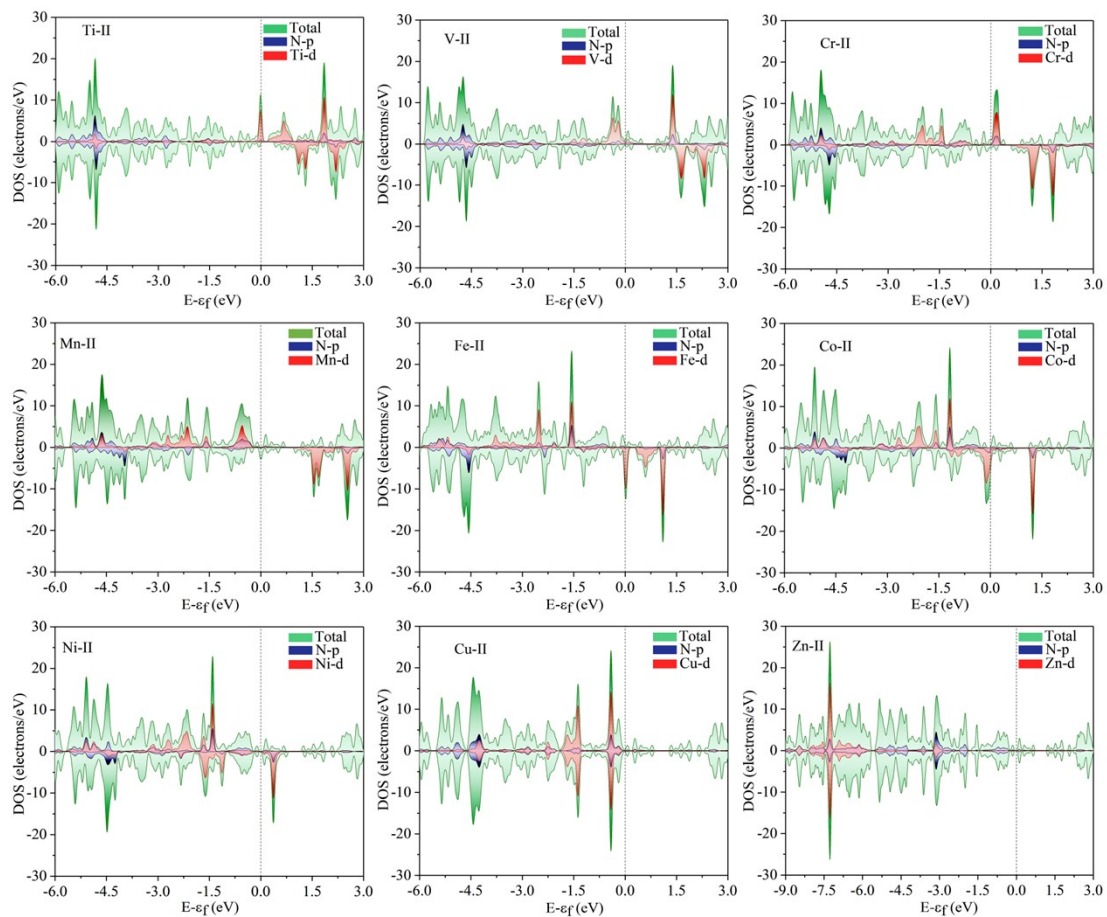
Figure S10. The DOS projected onto 4d TM-d and N-p orbitals and TDOS of TM-N$_3$(pyrrolic)-C (TM-II) electrocatalysts.

Table S2. The characteristics of CO_2 molecule physisorbed or chemisorbed on TM-N$_3$-C surfaces. Hirshflied charge (Q) distribution for C and O atoms of adsorbed CO_2 molecule on 36 TM-N$_3$-C catalysts, ΔQ_{CO2} representing charge that catalysts lose after CO_2 adsorption, the optimized geometric structure of adsorbed species (bond lengths of C-O and the bond angle of O-C-O), adsorption energy, and ICOHP value of M-C, M-O, C-O in which C and O are the atom of absorbed CO_2 specie. $\Delta Q_{CO_2} = Q_C + Q_{O_1} + Q_{O_2}$, in which Q_C, Q_{O_1}, and Q_{O_2} represent the Hirshfeld charge distribution for C and O atoms in adsorbed CO_2.

TM-N$_3$-C/isolated CO_2	Q_C (e⁻)	Q_{O1} (e⁻)	Q_{O2} (e⁻)	ΔQ_{CO2} (e⁻)	d_{C-O1} (Å)	d_{C-O2} (Å)	$\theta_{\angle OCO}$ (°)	E_{CO2} (eV)	ICOHP (eV/ M-C bond)	ICOHP (eV/M-O bond)	ICOHP (eV/C-O bond)
Ti-I	0.049	-0.216	-0.217	-0.384	1.351	1.207	132.282	-1.613	-2.863	2.679	-1.692
V-I	0.077	-0.184	-0.215	-0.321	1.331	1.206	135.519	-1.196	-3.069	1.666	1.563
Cr-I	0.064	-0.218	-0.204	-0.357	1.312	1.206	138.153	-1.020	-2.894	1.111	-2.894
Mn-I	0.109	-0.209	-0.177	-0.278	1.289	1.205	141.013	-0.835	-2.646	0.910	-0.423
Fe-I	0.140	-0.201	-0.156	-0.217	1.272	1.202	145.260	-1.005	-2.522	0.732	-1.334
Co-I	0.153	-0.190	-0.155	-0.192	1.254	1.202	147.617	-0.626	-1.838	0.326	-2.456
Ni-I	0.147	-0.205	-0.159	-0.217	1.265	1.203	146.263	-0.864	-2.358	0.469	-2.145
Cu-I	0.171	-0.158	-0.167	-0.154	1.234	1.194	153.993	-0.575	-2.087	0.816	-0.619
Zn-I	0.281	-0.132	-0.127	0.022	1.203	1.188	170.251	-0.026		-0.159	-2.857
Zr-I	0.023	-0.237	-0.245	-0.459	1.355	1.211	130.798	-1.863	-1.529	4.293	-1.439
Nb-I	0.036	-0.233	-0.232	-0.429	1.335	1.210	134.671	-1.702	-0.395	3.253	-2.451
Mo-I	0.070	-0.222	-0.200	-0.352	1.316	1.207	138.300	-1.400	-1.325	1.725	1.498
Tc-I	0.125	-0.212	-0.161	-0.248	1.284	1.205	141.635	-0.980	-2.190	1.364	-0.423
Ru-I	0.123	-0.182	-0.197	-0.256	1.244	1.206	149.028	-0.779	-1.171	0.852	-3.473
Rh-I	0.111	-0.201	-0.216	-0.306	1.265	1.204	144.262	-0.600	-2.337	1.118	-2.337
Pd-I	0.137	-0.198	-0.206	-0.267	1.228	1.199	152.533	-0.326	-1.524	0.962	-4.042
Ag-I	0.305	-0.138	-0.112	0.054	1.181	1.169	177.770	-0.300		-0.170	-4.136
Cd-I	0.260	-0.158	-0.157	-0.055	1.176	1.176	177.893	-0.090	-0.562	0.328	-4.020
Ti-II	0.105	-0.167	-0.177	-0.240	1.281	1.205	141.298	-0.653	-0.240	0.548	0.562
V-II	0.106	-0.153	-0.187	-0.234	1.287	1.204	141.300	-0.368	-0.234	0.396	1.066
Cr-II	0.093	-0.184	-0.183	-0.273	1.290	1.206	143.543	-0.129	-0.273	-0.120	-0.947
Mn-II	0.324	-0.095	-0.108	0.122	1.182	1.168	179.162	-0.276	0.122	-0.195	-3.994
Fe-II	0.316	-0.100	-0.109	0.107	1.192	1.179	178.611	-0.255	0.107	-0.180	-4.113
Co-II	0.311	-0.105	-0.114	0.092	1.181	1.169	178.471	-0.238	0.092	-0.242	-4.021

|											
Ni-II	0.292	-0.136	-0.132	0.025	1.177	1.172	179.014	-0.233	0.025	-0.070	-4.442
Cu-II	0.281	-0.144	-0.143	-0.007	1.175	1.174	179.303	-0.176	-0.007	0.098	-4.455
Zn-II	0.290	-0.144	-0.136	0.010	1.177	1.173	179.204	-0.201	0.010	-0.112	-4.398
Zr-II	0.075	-0.194	-0.186	-0.306	1.295	1.209	137.288	-1.016	-0.306	1.351	0.812
Nb-II	0.051	-0.197	-0.211	-0.357	1.304	1.208	138.185	-0.994	-0.357	0.856	1.750
Mo-II	0.082	-0.172	-0.199	-0.289	1.295	1.204	141.572	-0.711	-0.289	0.639	1.405
Tc-II	0.134	-0.158	-0.194	-0.218	1.254	1.207	146.800	-0.693	-0.218	0.317	-2.411
Ru-II	0.143	-0.183	-0.161	-0.200	1.238	1.200	150.368	-0.568	-0.200	0.252	-3.746
Rh-II	0.178	-0.159	-0.145	-0.126	1.228	1.192	154.779	-0.246	-0.126	0.521	-0.740
Pd-II	0.298	-0.156	-0.119	0.023	1.179	1.170	178.269	-0.301	0.023	-0.294	-4.002
Ag-II	0.296	-0.142	-0.126	0.028	1.178	1.171	178.221	-0.276	0.028	-0.117	-4.300
Cd-II	0.328	-0.115	-0.109	0.104	1.184	1.172	179.198	-0.227	0.104	-0.351	-3.956
isolated CO_2					1.176	1.176	180.000				-4.622
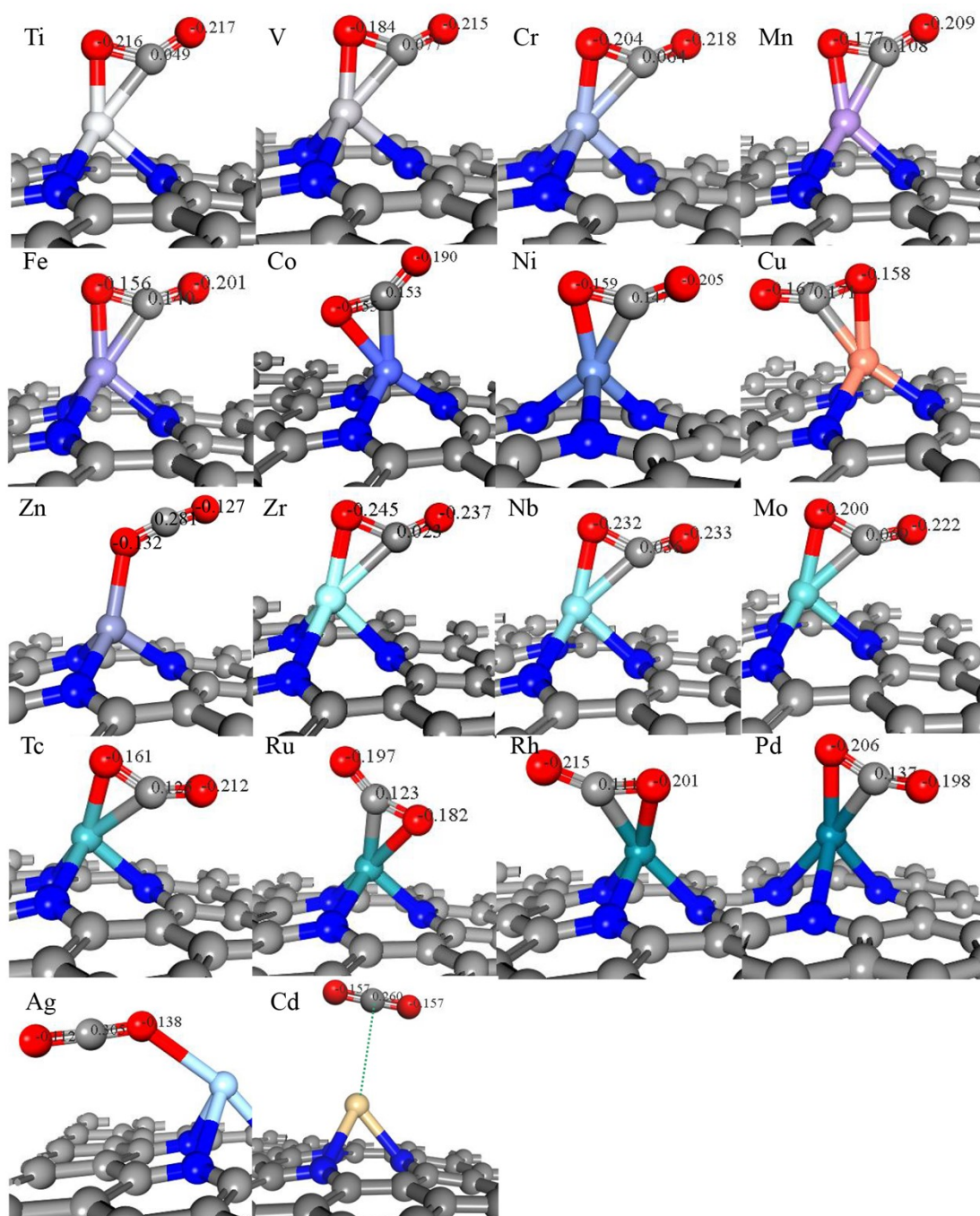
Figure S11. The side view of CO_2 adsorption structure with minimum energy on TM-I surfaces and the Hirshfeld charge analysis of adhered CO_2 species inserted. The colors of atoms are the same as Figure 2.
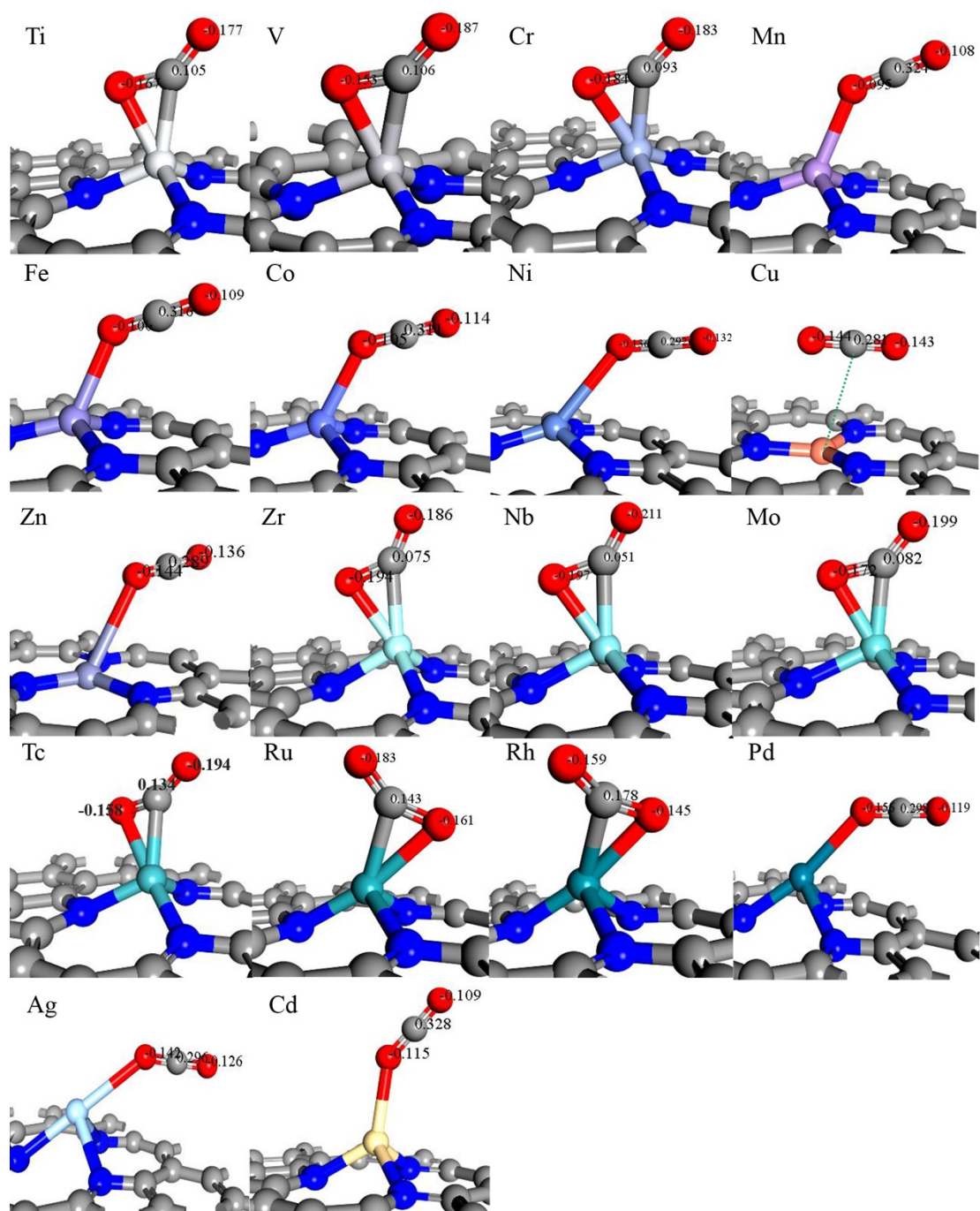
Figure S12. Optimized structures of CO_2 adsorbed on TM-II surfaces in which the Hirshfeld charge of the atoms for adhered CO_2 species were labeled. The colors of atoms are the same as Figure 2.

Figure S13. The crystal orbital Hamilton population (COHP) analysis of M-O (red), M-C (blue), and C-O (green) bond in which C and O means that the CO_2 were adsorbed on TM-I via C or O atoms. The ICOHP values are listed here, and ε_f represents the Fermi energy level.
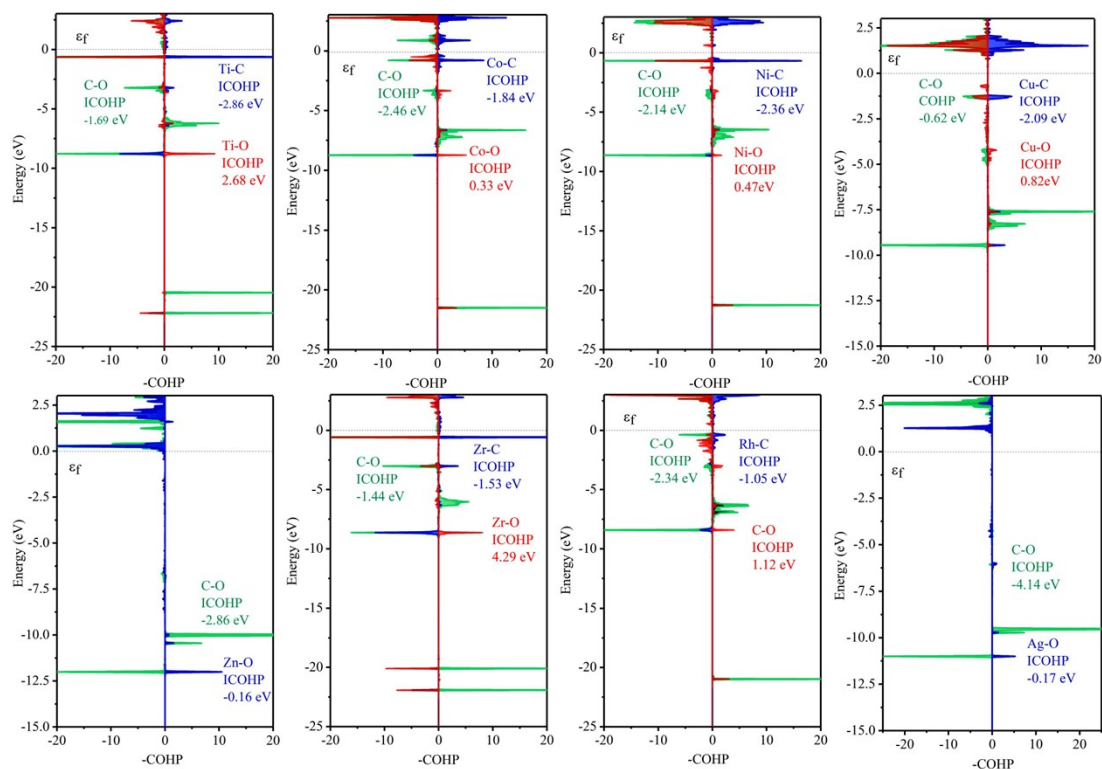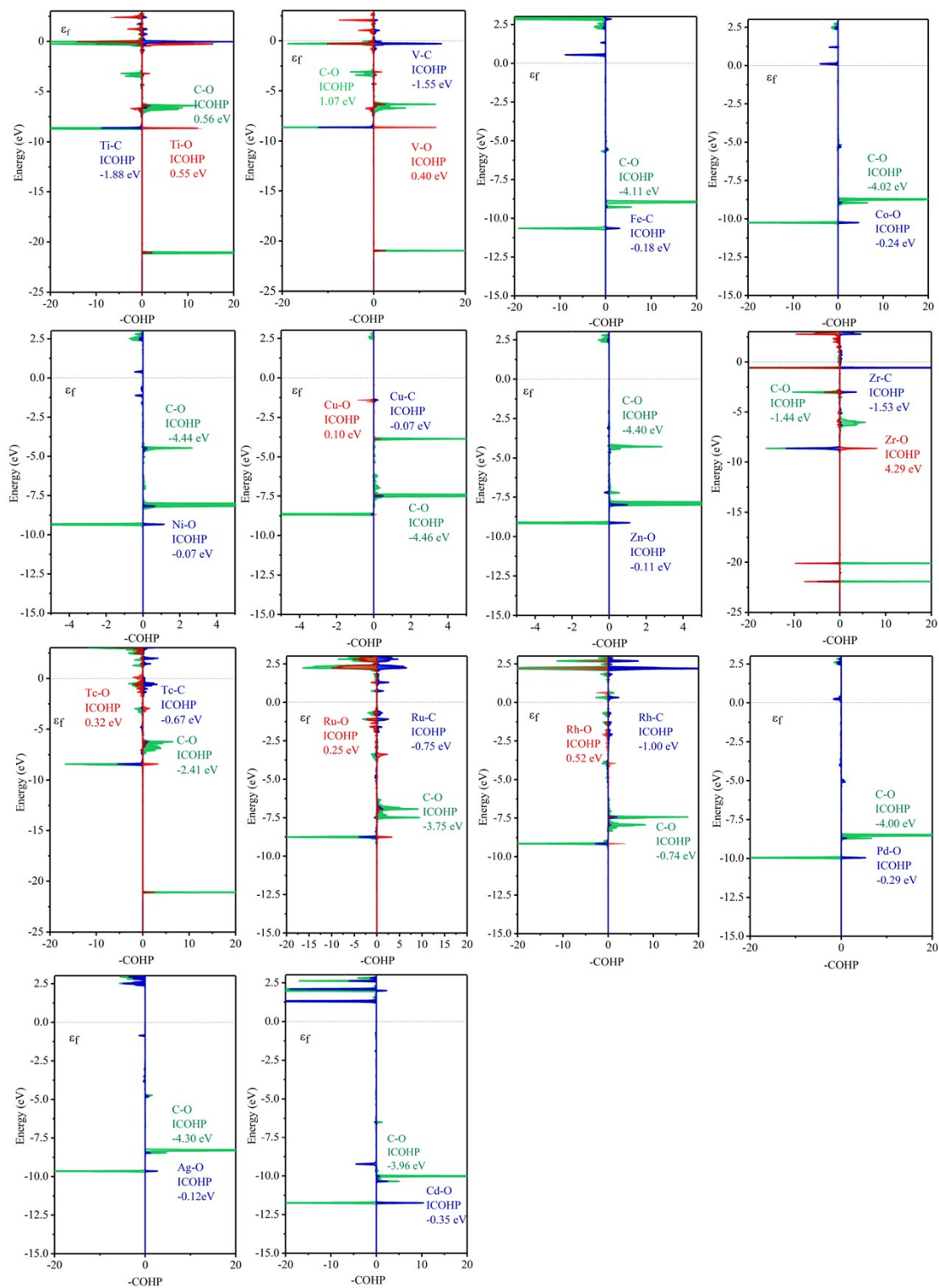
Figure S14. The crystal orbital Hamilton population (COHP) analysis of M-O (red), M-C (blue), and C-O (green) bond in which C and O means that the CO_2 were adsorbed on TM-II via C or O atoms. The ICOHP values are listed here, and ε_f represents the

Fermi energy level.

Table S3. The bond length between metal atoms and the O atoms from the *COOH, *CH$_2$OH and *CHO intermediates adsorbed on TM-N$_3$-C SACs.

| TM-N$_3$-C	M-O(*COOH)	M-O(*CHO)	M-O(*CH$_2$OH)
Ti-I	2.086	2.004	2.180
Co-I	2.172	2.120	2.038
Ni-I	2.267	2.090	2.027
Cu-I	2.742	2.785	2.775
Zn-I	2.839	2.851	2.775
Zr-I	2.227	2.146	2.299
Rh-I	2.649	2.638	2.324
Ag-I	2.967	3.012	2.993
Ti-II	2.109	2.018	2.203
V-II	2.068	2.080	2.209
Fe-II	2.710	2.773	2.728
Co-II	2.745	2.752	2.666
Ni-II	2.483	2.865	2.355
Cu-II	2.662	2.648	2.947
Zn-II	2.870	2.944	2.927
Zr-II	2.264	2.217	2.263
Tc-II	2.590	3.091	2.362
Ru-II	2.437	2.455	2.262
Rh-II	2.627	2.629	2.292
Pd-II	2.638	2.689	2.585
Ag-II	2.930	2.947	2.928
Cd-II	3.036	3.109	3.048
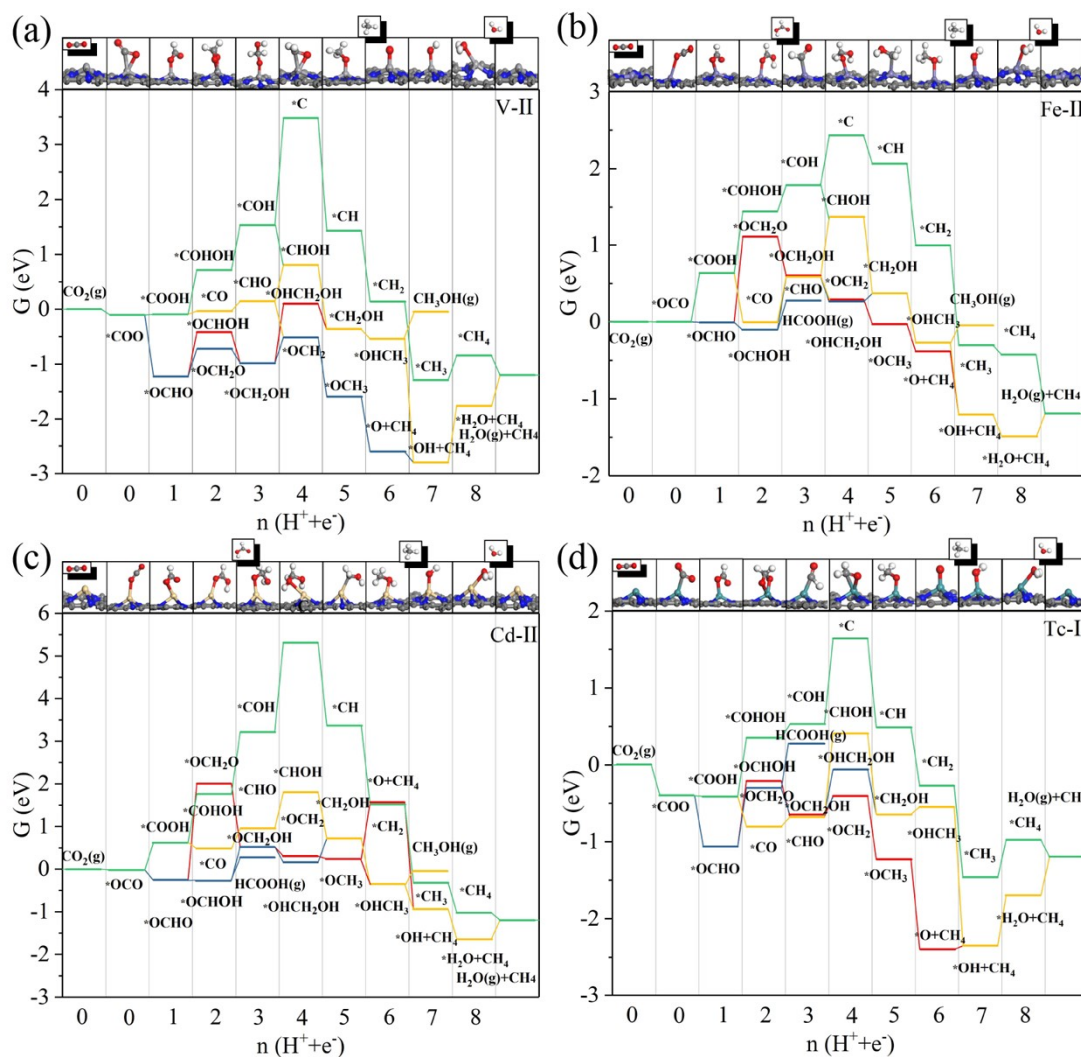
Figure S15. Free energy diagrams for electrocatalytic CO_2 reduction toward CH_4 product over (a) V-II, (b) Fe-II, (c) Cd-II, and (d) Tc-II SACs along possible elementary steps. The geometrical configuration of primary intermediates along the most favorable reaction pathways, and the productions of CO_2RR are shown as graphical insets, and the color scheme utilized is same as that applied in Figure S12.

Compared to Ti-I and Zr-I, the preferential pathway on Co-I with moderate outer shell electron numbers and electronegativity has the difference in second PCET steps, in which *OCHO was favorably conversed to *OCHOH instead of *OCH$_2$O. Next, the energy barrier of HCOOH desorption is higher than the free energy change of *OCHOH

22

-*OCH$_2$OH, resulting in continue hydrogenation of *OCH$_2$OH to CH$_4$ than the release of HCOOH molecules. The step determining reaction rate of CO$_2$RR is the second PCET step (*OCHO-*OCHOH) with the free energy change of 0.83 eV. The valence electron number and electronegativity of Ni is closely to Co, the prior pathway over Ni-I surface is the same with that on Co-I except for sixth PCET process, in which the conversion of *OCH$_3$ to *O is more advantageous to the reduction of *OCH$_3$ to *CH$_3$OH. Additionally, due to strong strength between adsorbed species (*OHCH$_3$) and active centers of Co-I, the desorption of CH$_3$OH (g) were well evade by the hydrogenation of *CH$_3$OH to generate *OH and release CH$_4$ molecule. Furthermore, the largest energy change of 0.75 eV for *OCHO-*OCHOH on the surface of Ni-I. Figure 5d shows that, on Cu-I surface, the dominant product was HCOOH for electrocatalytic CO$_2$RR with the free energy barrier of 0.46 eV, which would be generated via the following PCET reaction: *COO → *OCHO → *OCHOH. Moreover, if the overpotential of -0.63 V are applied in electrochemical CO$_2$RR, the CH$_4$ as side reaction will be generated along the following pathways: *COO → *OCHO → *OCHOH → *OCH$_2$OH → *OCH$_2$ + H$_2$O → *OCH$_3$ → *OHCH$_3$ → *OH + CH$_4$ → *H$_2$O. And for Zn-I, the CO$_2$-to-CH$_4$ reaction path and RDS (*OCHO-*OCHOH) are in common with that on Ni-I, in which the limiting potential for CO$_2$-to-CH$_4$ is -1.14 V. Compared Co-I to Rh-I with similar electronegativity and outer-shell electrons metal atoms, there was a little distinction in the free energy changes of the reduction of *OCHOH to *OCH$_2$OH or *CHO on Rh-I and Co-I, the primary third PCET step over Rh-I surface is the conversion of *OCHOH to *CHO. The step of *OCHO-*OCHOH

is RDS with free energy barrier of 0.81 eV on Rh-I. Unlike Rh-I, Co-I, Ni-I and Zn-I, it's found that, for Ag-I, the *OCHOH were reacted with one proton coupled with an electron transfer to form *CHO, simultaneously, which were hindered by the formation of HCOOH as dominant product for CO_2RR due to the much lower energy barrier of HCOOH desorption (0.29 eV) than the protonation of *OCHOH to *CHO (1.14 eV). Therefore, the possible pathway of CO_2-to-CH_4 reaction is depicted as follows: *OCHO → *OCHOH → *CHO + H_2O → *OCH$_2$ → *OCH$_3$ → *OHCH$_3$ → *OH + CH$_4$ → *H$_2$O, which were accompanied with vast formation of HCOOH. The formation rate for CH$_4$ and HCOOH on Ag-I were determined by the step of *OCHOH-*CHO and *OCO-*OCHO with -1.14 V and -0.54 V limiting potential, respectively.

We also found that the reaction pathways on Zr-II is identical to that on Zr-I during CO_2 reduced to CH$_4$, which is correspond with between Ti-I and Ti-II. In addition, for Zr-II, the step of *O transformed toward *H$_2$O is most difficult with the free energy barrier of 1.84 eV. Compared to Co-I, there are some differences of Co-II in the following aspects: 1) the reduction of *OCHOH to *CHO is easier than to *OCH$_2$OH, and the sixth protonation of *OCH$_3$ to *OCH$_3$OH is more advantageous, the preferential pathway for CO_2RR on Co-II is depicted as *OCHO → *OCHOH → *CHO + H$_2$O → *OCH$_2$ → *OCH$_3$ → *OHCH$_3$ → *OH + CH$_4$ → *H$_2$O; 2) It is more likely to release HCOOH molecule instead of the continue protonation of *OCHOH to *CHO because of a lower free energy barrier of 0.24 eV for HCOOH generation (versus 0.54 eV for the reduction of CO_2 to CH$_4$). For Ni-II as demonstrated in Figure 6c, it indicates that first protonation of *OCO gives priority to form *COOH, and then

*COOH was reduced to *CO that is likely to be desorbed from the surface of Ni-II than formation of *CHO in the next hydrogenation step. Moreover, CO is most primary production in the conversion of CO_2 to various C_1 products during CO_2RR and generated by the two proton-electron coupling reaction with 0.72 eV free energy barrier (*OCO-*COOH), which is conformity with previous experimental work. [20,21] Due to the uphill free energy step for *COOH-*CHO, the adsorbed *OCO were efficiently hydrogenated to CO with the help of multiple protons and electrons, resulting in hindering the formation of CH_4. Although the selectivity for CH_4 on the surfaces of Ni-II is extremely poor, the activity of CO_2RR is also investigated to revel the coordination environment effect. There are listed the most possible reaction pathways of CO_2 to CH_4 on Ni-II as shown: *COOH → *CO → *CHO → *OCH_2 →*OCH_3 →*OHCH_3 → *OH + CH_4 → *H_2O, in which RDS is also the elementary reaction step of *OCO-*COOH with U_L of -0.72 V. On Zn-II substrates, the isolated HCOOH molecules were efficiently generated during electrochemical CO_2RR because the proton-electron coupling process of CO_2-to-HCOOH (RDS: *OCO → *OCHO, 0.74 eV) was energetically beneficial than that of CO_2-to-CH_4 (RDS: *OCHOH → *OCH_2OH, 1.22 eV). We also found that the formation of CH_3OH is easier than CH_4 due to the spontaneous desorption of CH_3OH when the process of *OHCH_3 transformed to *OH need 0.32 eV energy. Compared Zn-I with Zn-II, it's also obviously found that the difference in hydrogenation path of OCH_2OH, i.e., *OCH_2OH → *OCH_2 → *OCH_3 for Zn-I and *OCH_2OH → *OHCH_2OH → *CH_2OH for Zn-II. Figure 5g and Figure 6g show the similar pathways between Rh-I and Rh-II except for the sixth PCET steps.

For Rh-II, the reduction of *OCH$_3$ to *OHCH$_3$ (-0.28 eV) is more favorable than the transformation of *OCH$_3$ to *O (0.08 eV). The reduction of *OCHO to form *OCHOH intermediates determine the rate of CO$_2$-to-CH$_4$ reaction, which require 0.55 eV to overcome energy barrier of the above process. Moreover, Figure 5h and Figure 6i demonstrate that both Ag-I and Ag-II perform the high selectivity for HCOOH of electrocatalytic CO$_2$RR, and the RDS step of them are both the hydrogenation of *OCO to *OCHO (0.54 eV and 0.99 eV). However, *CH$_2$OH is more likely to be formed than *OCH$_3$ on the surface of Ag-II during the fifth proton-coupled electron process, and then it prefers to generate CH$_3$OH molecules because of the uphill free energy step of reducing *OCH$_3$OH to *OH intermediates. Thus, for Ag-II, the HCOOH (0.99 eV) was the major product of CO$_2$RR, which was accompanied with trace production of CH$_3$OH & CH$_4$ at the limiting potential of -1.22 V. Compared to Rh-II, there are some differences in the primary reaction path of electrochemical CO$_2$RR on the surface of Ru-II due to different binding strength of adsorbed species and Ru and Rh metal sites. Furthermore, Figure 6 demonstrates that the two PCET reaction of reducing *OCHOH is likely to occur as the following steps: *OCHOH → *OCH$_2$OH → *OHCH$_2$OH, and the step of *OCHO-*OCHOH (0.51 eV) determines the reaction rate of electrochemical CO$_2$RR toward CH$_4$. As shown in Figure 6i, Pd-II electrocatalyst performs the higher activity of CO$_2$ reduction and superior selectivity for CH$_4$ with the limiting potential of -0.28 V.

Table S4. Rate determining step and limiting potential of TM-N$_3$-C electrocatalyst for CO$_2$RR toward CH$_4$ may accompanying side products as CO, HCOOH, or CH$_3$OH.

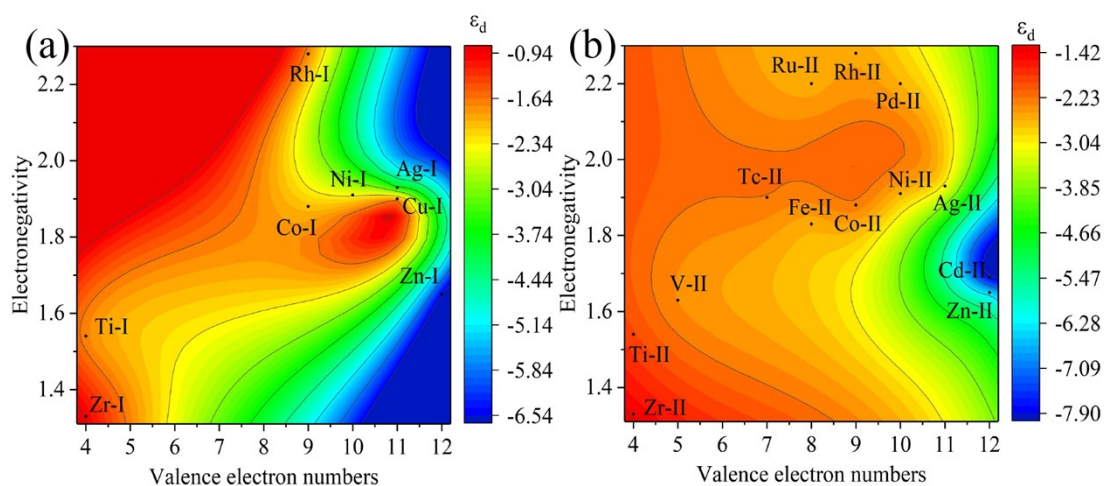| TM-N$_3$-C	CO$_2$RR toward CH$_4$		CO$_2$RR toward HCOOH		CO$_2$RR toward CO		CO$_2$RR toward CH$_3$OH	
	RDS	-U$_L$	RDS	-U$_L$	RDS	-U$_L$	RDS	-U$_L$
Ti-I	*OH-*H$_2$O	1.76						
Co-I	*OCHO-*OCHOH	0.83						
Ni-I	*OCHO-*OCHOH	0.75						
Cu-I	*OCHOH-*OCH$_2$OH	0.63	*OCHO-HCOOH(g)	0.46				
Zn-I	*OCHO-*OCHOH	1.14						
Zr-I	*OH-*H$_2$O	2.36						
Rh-I	*OCHO-*OCHOH	0.81						
Ag-I	*OCHOH-*CHO	1.14	*OCO-*OCHO	0.54				
Ti-II	*OH-*H$_2$O	0.95						
V-II	*OH-*H$_2$O	1.03						
Fe-II	*OCHOH-*CHO	0.69	*OCHO-HCOOH(g)	0.28				
Co-II	*OCHOH-*CHO	0.54	*OCHO-HCOOH(g)	0.24				
Ni-II	*CO$_2$-*COOH	0.72			*OCO-*COOH	0.72		
Cu-II	CO$_2$-*COOH	1.31			**CO$_2$-*COOH	1.31		
Zn-II	*OCHOH-*OCH$_2$OH	1.22	*+CO$_2$ -*OCHO	0.74			*OCHOH-*OCH$_2$OH	1.22
Zr-II	*OH-*H$_2$O	1.84						
Tc-II	*OCHO-*OCH$_2$O	0.75						
Ru-II	*OCHO-*OCHOH	0.51						
Rh-II	*OCHO-*OCHOH	0.55						
Pd-II	*CHO-OCH$_2$	0.28						
Ag-II	*OCHOH-*CHO	1.22	*OCO-*OCHO	0.99			*OCHOH-*CHO	1.22
Cd-II	*OCHOH-*OCH$_2$OH	0.79	*OCHO-HCOOH(g)	0.54				

Figure S16. The d band center maps for TM-I (a) and TM-II (b) as a function of the valence electrons number and electronegativity.

Table S5. The value of TM-N$_3$-C catalysts intrinsic characteristics including d-band center, electronegativity, and valence electron number of TM atoms.

| TM-N$_3$-C	ε_d(eV)	V_M	χ_M	Q_M (e$^-$)
Ti-I	-1.730	4	1.54	0.433
Co-I	-2.063	9	1.88	0.184
Ni-I	-2.393	10	1.91	0.201
Cu-I	-1.84	11	1.90	0.312
Zn-I	-6.52	12	1.65	0.295
Zr-I	-0.96	4	1.33	0.497
Rh-I	-1.75	9	2.28	0.242
Ag-I	-3.68	11	1.93	0.402
Ti-II	-1.94	4	1.54	0.494
V-II	-2.37	5	1.63	0.424
Fe-II	-2.58	8	1.83	0.320
Co-II	-2.27	9	1.88	0.238
Ni-II	-2.65	10	1.91	0.227
Zn-II	-6.45	12	1.65	0.428
Zr-II	-1.44	4	1.33	0.610
Tc-II	-2.24	7	1.90	0.317
Ru-II	-2.57	8	2.20	0.390
Rh-II	-2.54	9	2.28	0.357
Pd-II	-2.63	10	2.20	0.476
Ag-II	-3.11	11	1.93	0.355
Cd-II	-7.89	12	1.69	0.583
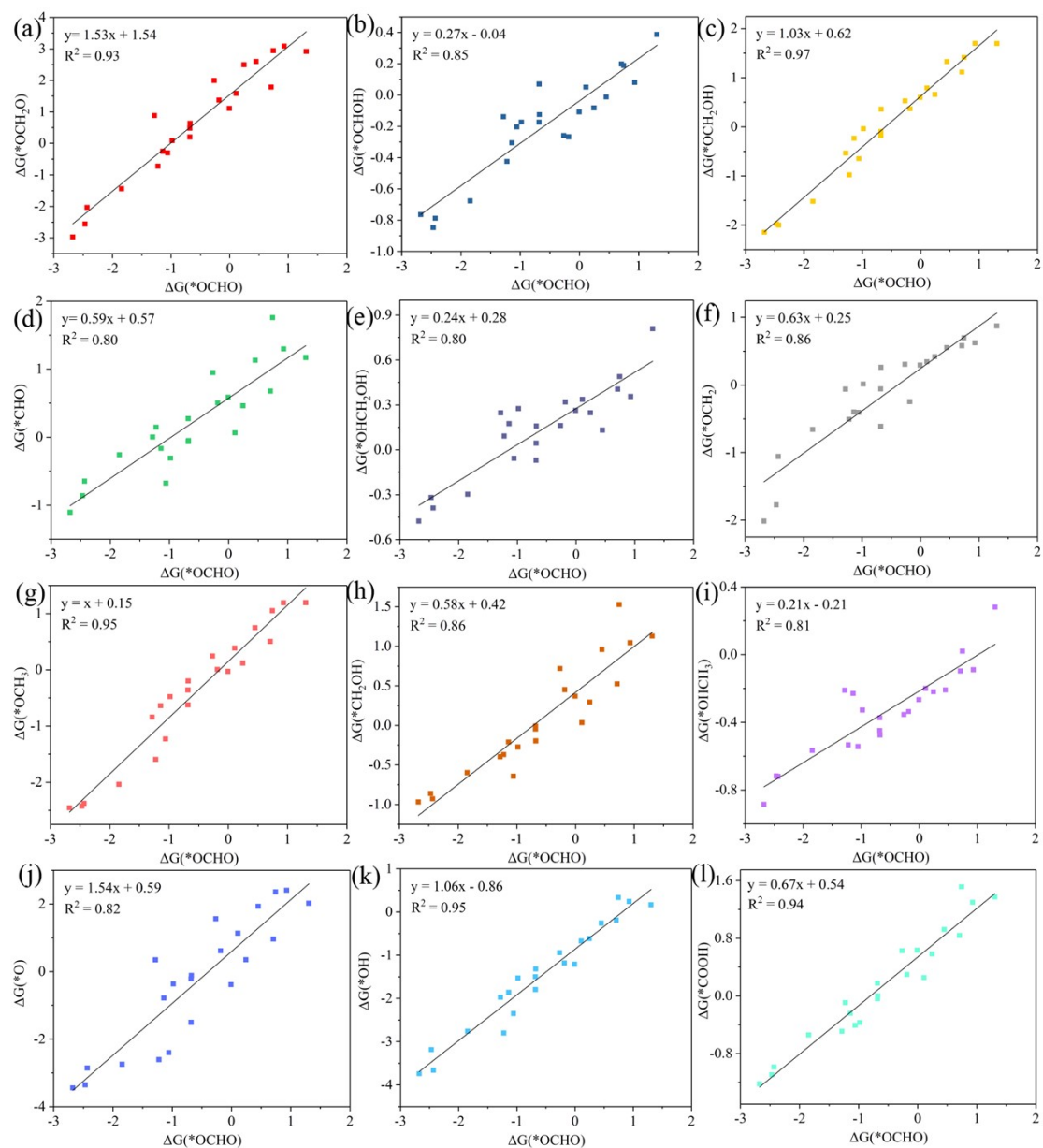
Figure S17. The adsorption Gibbs free energies of various intermediates along the preferred reaction pathways over TM-N$_3$-C catalysts as a function of that of *OCHO specie.
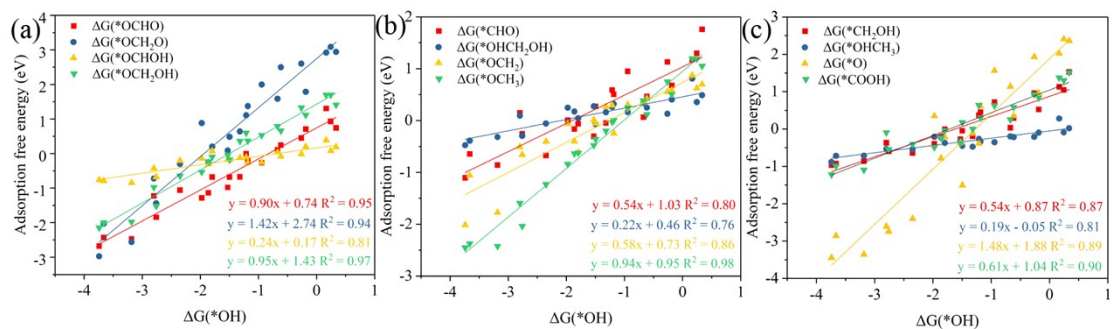
Figure S18. Scaling relationship between ΔG(*OH) and the adsorption free energies of O-bonded and C-bonded intermediates along the primary reaction pathways on TM-N$_3$-C surfaces.
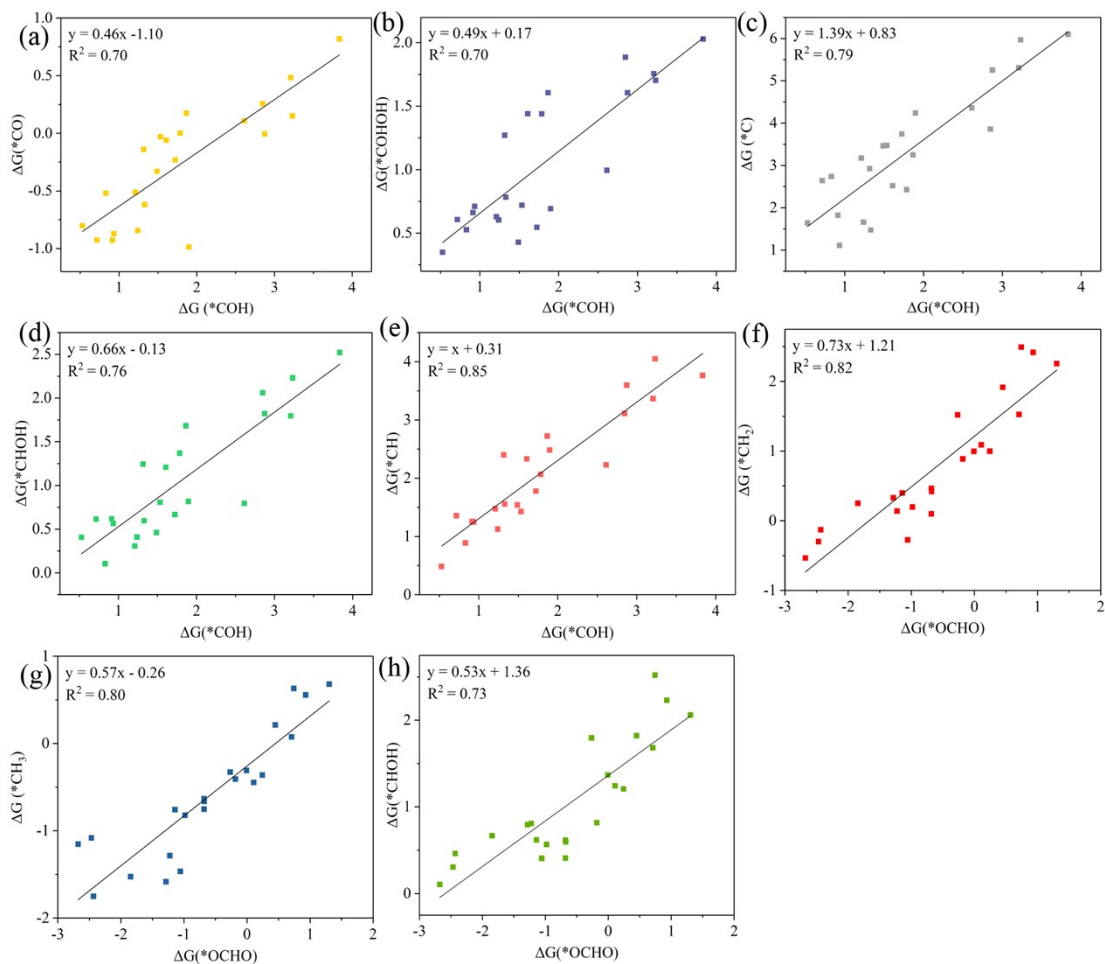

Figure S19. Adsorption free energies of all C-bonded intermediates over TM-N$_3$-C surfaces as a function of ΔG (*COH or *OCHO).
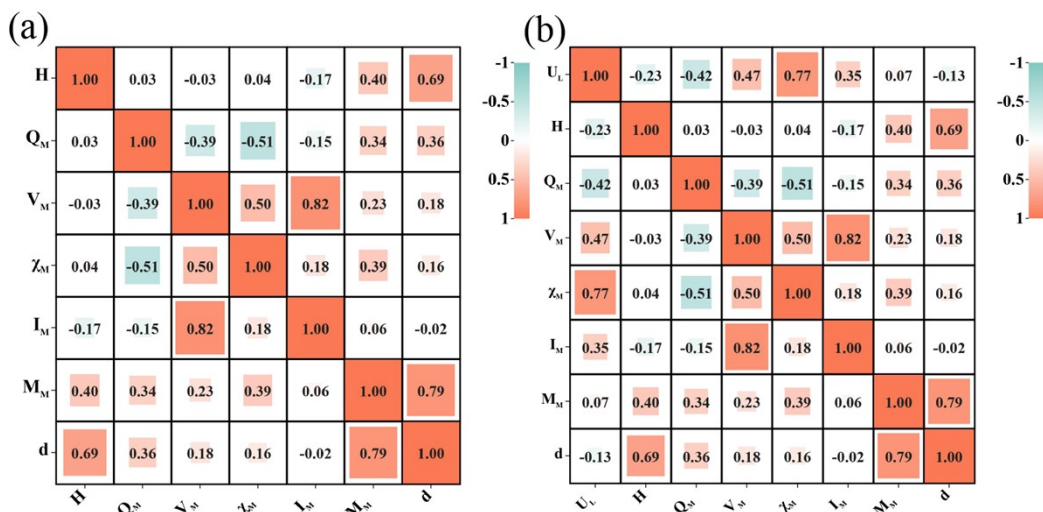
Figure S20. Correlation analysis of (a) the intrinsic characteristics of TM-N_3-C catalysts. (b) The correlation between Calculated U_L, H, Q_M, V_M, χ_M, I_M, M_M, and d.
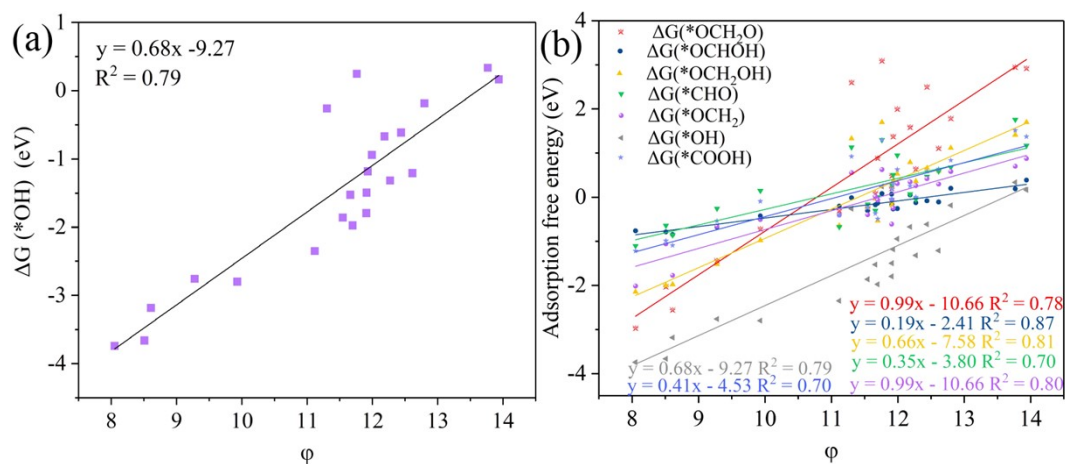

Figure S21. Adsorption free energies of (a) *OH and (b) all intermediates long the rate determining steps on TM-N_3-C surfaces as a function of the activity descriptor.

Table S6. The inherent characteristics of TM-N_4-C catalysts involving the bond length of M-N, the Hirshfeld charge of TM atoms, the valence electrons number, and the electronegativity, the intrinsic descriptor drawn by above features, $\Delta G(*OH)$ and the DFT-calculated U_L which is used to verify that the descriptor ψ can predict the activity of TM-N_4-C catalysts for electrocatalytic CO_2RR and selectivity for CH_4 generation.

TM-N_4-C	d_{M-N} (Å)	Q_M (e^-)	H (Å)	V_M	χ_M	ψ	$\Delta G(*OH)$	U_L
Ti-N_4-C	2.021	0.460	0.630	4.00	1.54	43.13	-3.65	-1.90
V-N_4-C	1.991	0.311	0.671	5.00	1.63	47.91	-2.87	-1.33
Cr-N_4-C	1.944	0.430	0.039	6.00	1.66	51.36	-1.58	-0.54
Mn-N_4-C	1.917	0.278	0.002	7.00	1.55	51.90	-1.06	-0.49
Fe-N_4-C	1.899	0.187	0.003	8.00	1.83	59.65	-0.98	-0.74
Co-N_4-C	1.887	0.061	-0.003	9.00	1.88	62.68	-0.53	-0.79
Ni-N_4-C	1.888	0.074	-0.003	10.00	1.91	64.56	0.40	-1.46
Cu-N_4-C	1.935	0.356	-0.001	11.00	1.90	63.70	0.23	-1.30
Zr-N_4-C	2.139	0.560	0.954	4.00	1.33	37.11	-4.11	-2.24
Nb-N_4-C	2.107	0.542	1.070	5.00	1.60	44.34	-3.96	-2.19
Ru-N_4-C	1.965	0.286	0.075	8.00	2.20	64.20	-0.83	-0.98
Rh-N_4-C	1.961	0.154	0.002	9.00	2.28	67.55	-0.67	-0.90
Pd-N_4-C	1.970	0.453	0.009	10.00	2.20	66.85	0.93	-1.70

References

1 B. Delley, *The Journal of Chemical Physics*, 2000, **113**, 7756–7764.

2 J. P. Perdew, M. Ernzerhof and K. Burke, *The Journal of Chemical Physics*, 1996, **105**, 9982–9985.

3 S. Grimme, *Journal of Computational Chemistry*, 2006, **27**, 1787–1799.

4 Z. Wang, J. Zhao and Q. Cai, *Phys. Chem. Chem. Phys.*, 2017, **19**, 23113–23121.

5 Q. Cui, G. Qin, W. Wang, K. R. Geethalakshmi, A. Du and Q. Sun, *Applied Surface Science*, 2020, **500**, 143993.

6 B. Delley, *Phys. Rev. B*, 2002, **66**, 155125.

7 J. Wang, M. Zheng, X. Zhao and W. Fan, *ACS Catal.*, 2022, **12**, 5441–5454.

8 X. Wang, H. Niu, Y. Liu, C. Shao, J. Robertson, Z. Zhang and Y. Guo, *Catal. Sci. Technol.*, 2020, **10**, 8465–8472.

9 H. Niu, X. Wang, C. Shao, Y. Liu, Z. Zhang and Y. Guo, *J. Mater. Chem. A*, 2020, **8**, 6555–6563.

10 Z. F. Zhang, T. G. Zhou, H. Y. Zhao and X. L. Wei, *Chinese Phys. B*, 2014, **23**, 016801.

11 R. Han, M. Qi, S. Dong, Z. Mao, X. Lin and P. Wu, *Physica E: Low-dimensional Systems and Nanostructures*, 2021, **129**, 114667.

12 A. Jalalinejad, M. Yeganegy, M. Farokhzad, M. Bagheri, A. Bahari and A. Gholizadeh, *Computational Condensed Matter*, 2021, **28**, e00575.

13 F. L. Hirshfeld, *Theoret. Chim. Acta*, 1977, **44**, 129–138.

14 Y. Zhou, L. Chen, L. Sheng, Q. Luo, W. Zhang and J. Yang, *Nano Res.*, 2022, **15**,

7994–8000.

15 J. K. Nørskov, J. Rossmeisl, A. Logadottir, L. Lindqvist, J. R. Kitchin, T. Bligaard and H. Jónsson, *J. Phys. Chem. B*, 2004, **108**, 17886–17892.

16 J. Greeley and J. K. Nørskov, *Electrochimica Acta*, 2007, **52**, 5829–5836.

17 X. Huang, L. Y. Gan, J. Wang, S. Ali, C. C. He, and H. Xu, *J. Phys. Chem. Lett.,* 2021, **12**, 9197−9204.

18 X. Guo, J. Gu, S. Lin, S. Zhang, Z. Chen and S. Huang, *J. Am. Chem. Soc.*, 2020, **142**, 5709–5721.

19 Y. Sun, J. Wang, Q. Liu, M. Xia, Y. Tang, F. Gao, Y. Hou, J. Tse and Y. Zhao, *J. Mater. Chem. A*, 2019, **7**, 27175–27185.

20 Q. Fan, P. Hou, C. Choi, T. Wu, S. Hong, F. Li, Y. Soo, P. Kang, Y. Jung and Z. Sun, *Adv. Energy Mater.*, 2020, **10**, 1903068.

21 J. Yang, Z. Qiu, C. Zhao, W. Wei, W. Chen, Z. Li, Y. Qu, J. Dong, J. Luo, Z. Li and Y. Wu, *Angewandte Chemie International Edition*, 2018, **57**, 14095–14100.